Monthly Notices of the ROYAL ASTRONOMICAL SOCIETY

MNRAS **525,** 1008–1022 (2023) https://doi.org/10.1093/mnras/stad2363
Advance Access publication 2023 August 4

Decomposing galaxies with BANG: an automated morphokinematic decomposition of the SDSS-DR17 MaNGA survey

Fabio Rigamonti [1,2,3★] Massimo Dotti,[2,3,4] Stefano Covino,[1,2] Francesco Haardt,[1,2,3] Luca Cortese [5,6] Marco Landoni[1,2] and Ludovica Varisco[3,4]

[1]*DiSAT, Università degli Studi dell'Insubria, via Valleggio 11, I-22100 Como, Italy*
[2]*INAF, Osservatorio Astronomico di Brera, Via E. Bianchi 46, I-23807 Merate, Italy*
[3]*INFN, Sezione di Milano-Bicocca, Piazza della Scienza 3, I-20126 Milano, Italy*
[4]*Dipartimento di Fisica G. Occhialini, Università di Milano-Bicocca, Piazza della Scienza 3, I-20126 Milano, Italy*
[5]*International Centre for Radio Astronomy Research, The University of Western Australia, Crawley, WA 6009, Australia*
[6]*ARC Centre of Excellence for All Sky Astrophysics in 3 Dimensions (ASTRO 3D), Australia*

Accepted 2023 July 28. Received 2023 July 4; in original form 2023 May 5

ABSTRACT

From a purely photometric perspective galaxies are generally decomposed into a bulge+disc system, with bulges being dispersion-dominated and discs rotationally supported. However, recent observations have demonstrated that such a framework oversimplifies complexity, especially if one considers galaxy kinematics. To address this issue we introduced with the GPU-based code BANG a novel approach that employs analytical potential-density pairs as galactic components, allowing for a computationally fast, still reliable fit of the morphological and kinematic properties of galaxies. Here we apply BANG to the SDSS-MaNGA survey, estimating key parameters such as mass, radial extensions, and dynamics, for both bulges and discs of +10 000 objects. We test our methodology against a smaller subsample of galaxies independently analysed with an orbit-based algorithm, finding agreement in the recovered total stellar mass. We also manage to reproduce well-established scaling relations, demonstrating how proper dynamical modelling can result in tighter correlations and provide corrections to standard approaches. Finally, we propose a more general way of decomposing galaxies into 'hot' and 'cold' components, showing a correlation with orbit-based approaches and visually determined morphological type. Unexpected tails in the 'hot-to-total' mass-ratio distribution are present for galaxies of all morphologies, possibly due to visual morphology misclassifications.

Key words: galaxies: disc – galaxies: kinematics and dynamics – galaxies: photometry – galaxies: statistics – galaxies: structure.

1 INTRODUCTION

Galaxies have been long studied using the 'bulge+disc' decomposition framework (see e.g. Mendel et al. 2014), with bulges thought to be spheroidal components with little net rotation, possibly originated via merger events and well described by the de Vaucouleurs surface brightness profile (De Vaucouleurs 1948), while discs are seen as the result of accretion and cooling of angular momentum conserving gas, typically described by a flat exponential profile supported by ordered rotation (Freeman 1970; White & Rees 1978).

Recent high-resolution observations have challenged such two-component decomposition. For instance, bulges are commonly divided into 'classical bulges' and 'pseudo-bulges', with the latter frequently showing disc-like features (see Laurikainen, Peletier & Gadotti 2016, for a review). To model this structural complexity, purely photometric decomposition methods and codes have been developed, initially working on 1D surface brightness profiles (e.g. Gavazzi et al. 2000), then applied to 2D images (e.g. GIM2D, by Simard et al. 2002) and including discs, bars (e.g. BUDDA, by de Souza, Gadotti & dos Anjos 2004), spiral arms, rings, and warps (e.g. GALFIT, by Peng et al. 2002).

In recent years, the development of integral field unit (IFU) spectroscopy has allowed for an unprecedentedly detailed description of the velocity field of galaxies, forcing the 'bulge+disc' decomposition to take into account also the observed kinematics; this has mainly been done by combining a photometry-assumed decomposition of the galaxy images with the extraction of each component kinematics from the spectra (Oh et al. 2016; Tabor et al. 2017).

These methods have been successfully applied on subsamples of surveys such as SAMI (Oh et al. 2016), MaNGA (Tabor et al. 2019), and CALIFA (Pak et al. 2021), helping us to disentangle and characterize the kinematic properties of bulges and discs. Relying and/or assuming a first decomposition based only on photometric data, these methods can inevitably introduce bias in any eventual extraction of kinematic information without guaranteeing any self-consistency between the density and the underlying gravitational potential.

An alternative approach is the orbit superposition method (Schwarzschild 1979), in which both the surface brightness and the line-of-sight kinematic observables are reproduced as the superposition of purposely weighted orbital families. In this method, the structural components of the galaxies are estimated ex-post the

★ E-mail: frigamonti@uninsubria.it

fit, associating orbits to bulge and disc components depending on their angular momentum and spatial extension (Zhu et al. 2018b, c). Despite the strength and the generalization capabilities of these methods, their applicability is limited by the huge computational power required for orbits integration and weighting.

In a former paper (Rigamonti et al. 2022b, hereinafter Paper I), we proposed a new approach to this problem that lies between the purely photometric decomposition methods and the orbit-based ones. To this aim, we developed and publicly released BANG[1], a GPU-optimized code aimed at a fully Bayesian estimation of the global structure of disc galaxies. BANG performs a nested sampling analysis (Skilling 2004), assuming that each galaxy is composed of simple 'classical' components, such as a bulge and one or more discs, parametrized in terms of analytic density distributions and characterized by well-defined dynamics. In Paper I, as a case study, we applied BANG to NGC 7683, an S0 galaxy carefully selected for its regular velocity pattern and disc-like geometry, finding substantial agreement with the orbit-based code DYNAMITE (Jethwa et al. 2020) at a fraction of the computational cost despite the fact that the number of models explored by BANG far exceeds the orbit-based galaxy realizations.

Motivated by the first success of our effort, we decided to apply an updated version of BANG to a large sample of galaxies, namely, the full SDSS-DR17 MaNGA survey (Abdurro'uf et al. 2022), consisting in $+10\,000$ local ($0.01 \lesssim z \lesssim 0.1$) galaxies with IFU data. This paper is the first of a series describing our study and findings, and it is structured as follows. In §2 we briefly set out the sample we analysed, in §3 we summarize the methodology upon which BANG is based. §4 is devoted to the analysis of a single galaxy as a showcase, while in §5 we perform a comparison of BANG results for a selected subsample to orbit superposition methods. Our novel methodology is then applied to the whole MaNGA sample in §6 highlighting some preliminary results. In §7 we show scaling relations in comparison to similar existing studies, while §8 is devoted to summary and discussion about follow-up studies.

2 DATA SAMPLE

This study is based on a morphokinematic data set built upon the SDSS imaging survey (Strauss et al. 2002) and the final release of the MaNGA survey from the Seventeenth Data Release (DR17; Abdurro'uf et al. 2022) of the fourth phase of the Sloan Digital Sky Survey (SDSS-IV; Blanton et al. 2017). In the following, we briefly describe the most relevant features of these surveys and their data reduction pipelines.

2.1 Kinematics: the MaNGA survey

The Mapping Nearby Galaxies at Apache Point Observatory (MaNGA) survey (Bundy et al. 2015; Drory et al. 2015) has collected integral field spectroscopic measurements for $+10\,000$ local galaxies selected to have a roughly flat stellar mass distribution above 10^9 $M_\odot$ in the redshift range $0.01 < z < 0.15$. The IFUs observations have been carried out with different setups ranging from 19 IFU-fibre bundles ($\simeq 12$ arcsec diameter) to 127 IFU-fibre bundles ($\simeq 32$ arcsec diameter). The adopted configuration changes depending on different galaxy properties, we refer to Wake et al. (2017) for more details about the selection criteria and the distribution of the IFU sizes. The MaNGA survey is divided into a primary sample ($\simeq 67$ per cent) consisting of galaxies observed up to 1.5 R_e and a secondary sample ($\simeq 33$ per cent) with spatial coverage of 2.5 R_e. The raw data are collected after a $\simeq 3$ h-long dithered exposure and reduced by the data reduction pipeline (Law et al. 2016; Yan et al. 2016). The reduced data cubes contain a spectrum at each spatial element with a resolution $R \simeq 2000$ (i.e. $\sigma_{inst} \simeq 70\,km\,s^{-1}$) in the wavelength range 3600–10 000 Å. During each exposure, the hexagonal plate of the IFU is subject to dithered movements resulting in a datacube binned to a 0.5 arcsec grid in order to optimally sample the 2.5 arcsec full width at half-maximum (FWHM) reconstructed point spread function (PSF) (Westfall et al. 2019). In addition to each data cube, the MaNGA collaboration provides a data analysis pipeline (DAP; Belfiore et al. 2019; Law et al. 2021) comprising a set of spatially resolved maps in different configurations depending on the spatial binning and on the stellar templates adopted in the data-cube spectral fitting process (see Westfall et al. 2019 for further details). In this work, we collected, through the DAP web interface MARVIN (Cherinka et al. 2019), line of sight (l.o.s.) stellar velocity and velocity dispersion estimates and their associated errors assuming the same spatial binning as for the data cube. For each galaxy, we discarded all the pixels with S/N<4 (<6) for the velocity (velocity dispersion) to avoid spurious data in the outskirt of galaxies. On top of this, we applied the isolation forest algorithm (Liu, Ting & Zhou 2012) to each of the two maps to further mask possible outliers still present especially in the outskirt of velocity dispersion data.

2.2 Photometry: the SDSS survey

The observed MaNGA galaxies are a small subsample drawn from the SDSS imaging survey for which a wealth of ancillary information is available. For each MaNGA galaxy, we downloaded the original *i* and *g* band (10 arcmin × 13 arcmin) SDSS (DR17; Abdurro'uf et al. 2022) brightness maps and cropped them to the same spatial extension and resolution of the MaNGA kinematics squared cut-outs[2] using the procedure discussed in Bertin et al. (2002). We then computed the associated error by considering a Poissonian statistics on the number of detected photo-electrons and the contribution of additional sources of noise (i.e. read-noise and noise in the dark current).[3] We then converted, by knowing the galaxy redshift, the photometric maps to astrophysical units ($L_\odot\,kpc^{-2}$) and masked the possible presence of stars using DAOStarFinder, a PYTHON package based on the Stetson (1987) implementation, combined with the isolation forest algorithm mentioned above. This procedure has been automated and applied to all the MaNGA galaxies in both the *i* and *g* bands allowing us to compute estimates of the stellar mass-to-light ratio (M/L) from standard colour–M/L relation (Zibetti, Charlot & Rix 2009). The associated error, computed by propagation, is generally large enough to account for the scatter of the linear relation and for any assumption on the initial mass function. M/L ratio data are masked following the same procedure as done in the case of the velocity dispersion. In the end, we obtained a data set comprising spatially resolved information of brightness, M/L, l.o.s. velocity, and velocity dispersion of 10 005 galaxies morphologically

[1] https://pypi.org/project/BANGal/

[2] Note that the Manga square cut-outs always exceed the hexagonal region for which IFU data are available. Since it is not obvious how to limit the region within which brightness measurements are considered for large galaxy samples, we chose to never exceed the MaNGA squared cut-outs and to mask all the pixels outside an ellipse containing more than 60 noisy (i.e. NaN) measurements.

[3] See https://dr12.sdss.org/datamodel/files/BOSS_PHOTOOBJ/frames/RERUN/RUN/CAMCOL/frame.html for further details about the computation of the photometric errors.

characterized according to the classification presented in the MaNGA Visual Morphology Catalogue (VMC-VAC; Vázquez-Mata et al. 2022).

3 METHODOLOGY

For each galaxy, we fit simultaneously the logarithm of the *i*-band brightness, the stellar M/L, the velocity (v_{los}), and the l.o.s. velocity dispersion (σ_{los}) using an upgraded version of BANG (Rigamonti et al. 2022a). In the following, we will briefly summarize the main assumption underlying our dynamical model, the assumed priors, and the adopted criteria for selecting among different models. To perform this study we extensively used high-performance computing resources dividing our samples into groups of 20 galaxies and iteratively analysing them with a multi-GPU parallelization strategy; the average duration of each GPU job was $\simeq$ 12 h ($\simeq$ 30 min per galaxy) implying a total amount of $\simeq$ 6000 GPU h^{-1} per sample run.

3.1 Model

Each galaxy is the superposition of a spherical bulge, two exponential razor-thin discs and a dark-matter halo. Each model is axially symmetric and has a well-defined centre that corresponds to both the photometric and dynamical centre shared by all the components.

(i) The bulge is assumed to be spherically symmetric with an isotropic velocity distribution described, differently from what is assumed in Paper I, by a Dehnen profile (Dehnen 1993). The l.o.s. projected quantities, namely the surface density (Σ_b) and the velocity dispersion (σ_b) at any location in the plane of the sky R, are:

$$\Sigma_b(R) = \frac{M_b R_b (3-\gamma)}{2\pi} \int_R^\infty \frac{r^{1-\gamma}}{(r+R_b)^{4-\gamma}} \frac{\mathrm{d}r}{\sqrt{r^2-R^2}}, \quad (1)$$

$$\sigma_b^2(R) = \frac{(3-\gamma) G M_b^2 R^2 R_b}{4\pi\,\Sigma(R)} \int_R^\infty \frac{r^{1-2\gamma}}{(r+R_b)^{7-2\gamma}} \frac{\mathrm{d}r}{\sqrt{r^2-R^2}}, \quad (2)$$

where M_b and R_b are the mass and the scale radius of the bulge while γ is the inner slope of the density profile.

(ii) The inner and the outer discs are modelled as exponential razor-thin discs whose intrinsic velocity dispersion and tangential velocity are approximated assuming that a fraction k_j (with the convention of $j = 1$ for the inner disc and $j = 2$ for the outer disc) of the total kinetic energy is in ordered bulk motion and the rest goes into an isotropic velocity dispersion component. The 'kinematic decomposition parameter' k_j is a free parameter of the model. Its value ranges from $k_j = 0$ for a dispersion-supported regime to $k_j = 1$ for a rotation-supported regime. More specifically, the bulk l.o.s. velocity component for each disc is

$$v_{d,j}(R) = -k_j \, \sin i \, \cos\phi \, v_c(r), \quad (3)$$

where r is the deprojected distance from the centre of the galaxy of the R position, ϕ is the azimuthal angle evaluated in the plane of the disc from the major axis of the projected disc, and v_c is the total circular velocity.

The l.o.s. velocity dispersion of the disc is instead

$$\sigma_{d,j}^2(R) = \left(1 - k_j^2\right) \frac{v_c^2(r)}{3}, \quad (4)$$

where the factor 3 at the denominator is due to the assumption of an isotropic velocity dispersion tensor. As discussed in Paper I, the assumption of razor-thin discs is inconsistent with having a finite velocity dispersion; still, the effect on the fit is small as long as the discs have aspect ratio $\lesssim 0.1$.

(iii) The dark matter halo is described by a Navarro–Frenk–White profile (Navarro, Frenk & White 1996) with a cut-off radius R_{200} equals to the distance at which the mean density corresponds to 200 times the cosmological critical density. The circular velocity associated to the dark matter contribution to the total potential reads:

$$v_h^2(r) = \frac{G M_h}{r} \frac{\log(1+r/a) - r/(r+a)}{\log(1+c) - c/(1+c)}, \quad (5)$$

where M_h is the halo mass, c is the concentration, and a is the halo scale radius computed as R_{200}/c. Within our fitting strategy, we parametrized the halo mass in terms of the logarithm of the ratio between the dark and the visible mass $\log_{10} f_\star$.

SDSS *i*-band image data and MaNGA kinematics come with different PSFs, with an average of about 1.2 arcsec and 2.5 arcsec, respectively. To avoid any loss of information in the data, we accounted for different PSF convolutions between the photometry and the kinematic, considering for each galaxy the actual PSF FWHM as provided by the SDSS ancillary data and the MaNGA DAP catalogue. For this analysis, we successfully fitted 10 005 galaxies with three possible components configurations, namely a bulge+disc+disc ('B + D_1 + D_2') model, a bulge+disc ('B + D_1') model, and a disc+disc ('D_1 + D_2') model, whose parameters are summarized in Table 1. For each galaxy we selected the best-fitting model as the one with the highest evidence, resulting in $\simeq$ 86 per cent of the sample preferring the 'B + D_1 + D_2' model, $\simeq$ 6 per cent the 'B + D_1' model, and the remaining $\simeq$ 8 per cent the 'D_1 + D_2' model.

3.2 Priors

Our Bayesian approach requires the inclusion of any a priori knowledge of the probability distribution of each model parameter. In our case, since we are dealing with a statistically large sample of galaxies, it is mandatory to assume well-motivated representative priors. Given the complex nature of the problem at hand, we assumed different levels of priors combining information from both simulations and theoretical predictions. We emphasize that our modelling scheme significantly deviates from any other approach employed in the study of galactic dynamic decomposition, particularly when it comes to analysing such a large sample of objects while also considering kinematic information. This is the reason why we have not taken into account observational priors, which are typically derived solely from photometric decomposition and thus not aligned with our methodology. We also stress that in the majority of cases, where the data provide sufficient information, our results are in fact independent of the assumed priors.

(i) **Strong prior**

Using the output from a z=0 snapshot of the TNG50 simulation (Nelson et al. 2019; Pillepich et al. 2019), we estimated a relation between the total stellar mass ($M_\star$) and the halo mass (M_h) (see the next bullet point for a detailed description on how these mass estimates have been obtained). Moreover, following previous works in the literature (Cappellari et al. 2013; Zhu et al. 2018a; Jin et al. 2020), we assumed a relation between the halo mass and its concentration following estimates from Dutton & Macciò (2014). For both the halo mass and its concentration parameter we opted for two different fitting set-ups. In both cases, we still assumed 2D Gaussian priors respectively centred around the assumed relations ($M_\star - M_h$ and $M_h - c$), but in a second, more conservative approach we do not allow for halo parameter exploration outside 1-σ of the assumed relation. We refer to the two cases respectively as 'halo-

Table 1. Summary of the model parameters in the three different configurations, namely a bulge+disc+disc ('B + D_1 + D_2'), a bulge+disc ('B + D_1'), and a disc+disc ('D_1 + D_2') model. The first two columns describe each parameter and its reference name used in this work. Columns three, four, and five visually represent the inclusion of the parameters in the different models, while the last column describes the adopted prior ranges. When not differently specified positions, masses, angles, and mass-to-light ratios are respectively normalized to kpc, $M_\odot$, degrees, and $M_\odot/L_\odot$. We refer to Section 3.2 for a more detailed discussion about the assumed priors.

Description	Name	'B + D_1 + D_2'	'B + D_1'	'D_1 + D_2'	Prior range
Horizontal/vertical position of the centre	x_0; y_0	✓	✓	✓	[−2,2]
Position angle	P.A.	✓	✓	✓	[−180,180]
Inclination angle	i	✓	✓	✓	[3,87]
Mass, scale radius, and inner slope of the bulge	$\log_{10}M_b$; $\log_{10}R_b$; γ	✓	✓	×	[7.75,13.0], [−2,2], [0,2]
Mass and scale radius of the inner disc	$\log_{10}M_{d,1}$; $\log_{10}R_{d,1}$	✓	✓	✓	[7.75,13], [−2,2]
Mass and scale radius of the outer disc	$\log_{10}M_{d,2}$; $\log_{10}R_{d,2}$	✓	×	✓	[7.75,13], [−2,2]
Halo-to-stellar mass fraction and concentration	$\log_{10}f_\star$; c	✓	✓	✓	[0.1,2.7], [1,20]
Mass-to-light ratio of the bulge	$(M/L)_b$	✓	✓	×	[0.1,20]
Mass-to-light ratio of the inner disc	$(M/L)_{d,1}$	✓	✓	✓	[0.1,20]
Mass-to-light ratio of the outer disc	$(M/L)_{d,2}$	✓	×	✓	[0.1,20]
Kinematic decomposition parameter of the inner disc	k_1	✓	✓	✓	[0.01,1]
Kinematic decomposition parameter of the outer disc	k_2	✓	×	✓	[0.01,1]

free' and 'halo-fixed' configurations, we anticipate that generally, the two approaches lead to similar results in terms of the estimated stellar parameters.

(ii) **Mild-informative prior**

We assumed prior relations among the following pairs of model parameters: (M_b, $R_{b-\mathrm{half}}$), (M_{d1}, $R_{d1-\mathrm{half}}$), (M_{d2}, $R_{d2-\mathrm{half}}$), where the 'half' subscript refers to the half-mass radius of that component. Starting from a z=0 snapshot of the TNG50 simulation (Nelson et al. 2019; Pillepich et al. 2019), we collected masses and half-mass radii for bulges, discs, and haloes of a representative sample of simulated galaxies analysed with MORDOR[4] (Zana et al. 2022), a publicly available code which decomposes galaxies in their structural components depending on the energy and angular momentum of the stellar distribution. Note that this methodology, being phase-space based, allow us to include prior information in the most consistent way with BANG. For each galaxy component analysed by MORDOR, we estimated scaling relations for the above-mentioned parameter pairs by computing the average and standard deviation in different mass bins. We stress that, in our fitting approach, we do not force those parameters to strictly obey the simulated-obtained relations, instead, we included that additional information as a Gaussian prior on the considered radii whose dispersion does depend on the mass of the component such that any parameter pair is still free to converge possibly far away from the assumed relation.

(iii) **Uninformative prior**

We assumed uniform or log-uniform prior for most of the parameters over a range broad enough to account for the large variability present in our sample. Similarly to what was done in Paper I, we adopted a prior proportional to the sine of the inclination angle for disc-like galaxies (S and S0) while a flat distribution is assumed in the case of ellipticals. We summarize the adopted choices in the 6th column of Table 1

3.3 Caveats

Before any further analysis, we discuss some caveats regarding our methodology.

In $\simeq$ 15 per cent of the cases, the spherical bulge is almost not resolved, with a half-mass radius, even if generally affected by large errors, well below the pixel resolution. It is possible that in some circumstances this indicates the presence of a sub-nuclear structure, even though, more probably, it is an effect arising either from some limitations of our modelling scheme or from spurious features in the central regions of the data. This happens only in models made up of three visible components and it roughly anticorrelates with the model evidence, meaning that for small bulges, generally the evidence difference between the three visible components model and the two visible components one generally decreases. As we will discuss again in Section 6 this should not affect our analysis in terms of the proposed decomposition.

The brightness spatial extension is typically larger than the field of view covered by the kinematics. It is not obvious where to stop including brightness measurements, especially if the process must be automated for many galaxies. Our choice is never to exceed the squared MaNGA cut-outs and to mask all the pixels outside an ellipse containing more than 60 noisy (i.e. NaN) measurements. This approach generally prevents our fits to be affected by brightness noise-dominated regions, even though, in some cases, our estimates converge towards unrealistically extended discs (for 'D_2' only); similarly to what is discussed for the bulge, this happens only for a three visible components model. As a conservative approach, in these cases, when the disc scale radius ($R_{d,2}$) is larger than $2.5R_e$,[5] we replace the total mass of the external disc with the mass within $2.5R_e$. For the forthcoming analysis we adopt R_e as provided by the MaNGA DAP (Blanton et al. 2011).

Before moving to discuss our results, it is important to stress the main focus of our work. Galaxy automated decomposition can sometimes lead to incorrect classification of the components. In fact, some confusion can arise between classical bulges, pseudo-bulges, and bars. Similarly, degenerations can arise between extended bars and galactic thin and thick discs (Kormendy & Kennicutt 2004; Erwin et al. 2015; Kruk et al. 2018). At present, our model is not complex enough to account for such a detailed description. It must be said that it is not clear whether the current spatial and spectral resolution of the largest IFS surveys (i.e. MaNGA) is sufficient to break the degeneracy between these components. None the less, we argue that including kinematics in the decomposition, as we do in this work,

[4] https://github.com/thanatom/mordor

[5] Which roughly corresponds to the maximum region probed by the MaNGA kinematics.

Table 2. Results of the fit over the 1–256009 galaxy. The first column is the name of the parameter while the second and the third columns refer the best-fitting value and the errors, estimated as the 50th, the 95th, and the 5th percentiles of its marginalized posterior distribution, respectively in the 'halo-fixed' and 'halo-free' configurations.

Parameter	Halo-fixed	Halo-free
x_0(kpc)	$0.227^{+0.002}_{-0.003}$	$0.225^{+0.002}_{-0.002}$
y_0(kpc)	$0.244^{+0.002}_{-0.002}$	$0.245^{+0.002}_{-0.002}$
P.A.(deg)	$22.6^{+0.2}_{-0.2}$	$22.7^{+0.2}_{-0.2}$
i	$50.7^{+0.3}_{-0.3}$	$50.7^{+0.3}_{-0.3}$
$\log_{10}(M_b/M_\odot)$	$10.69^{+0.01}_{-0.02}$	$10.73^{+0.01}_{-0.01}$
$\log_{10}(R_b$/kpc)	$-1.05^{+0.04}_{-0.04}$	$-0.96^{+0.03}_{-0.03}$
γ	$0.06^{+0.14}_{-0.06}$	$0.06^{+0.14}_{-0.06}$
$\log_{10}(M_{d,1}/M_\odot)$	$10.89^{+0.01}_{-0.01}$	$10.87^{0.01}_{0.01}$
$\log_{10}(R_{d,1}$/kpc)	$0.20^{+0.01}_{-0.01}$	$0.26^{+0.01}_{-0.01}$
$\log_{10}(M_{d,2}/M_\odot)$	$10.79^{+0.02}_{-0.02}$	$10.76^{+0.03}_{0.04}$
$\log_{10}(R_{d,2}$/kpc)	$0.95^{+0.01}_{-0.01}$	$1.11^{+0.02}_{-0.02}$
$\log_{10}(f)$	$1.94^{+0.01}_{-0.01}$	$1.8^{+0.2}_{-0.1}$
c	$7.81^{+0.02}_{-0.03}$	$10.0^{+1}_{-1.3}$
$\log_{10} M_{h,5}/M_\odot$	$12.15^{+0.02}_{-0.02}$	$12.38^{+0.06}_{-0.05}$
$(M/L)_b[M_\odot/L_\odot]$	$2.8^{+0.2}_{-0.2}$	$3.2^{+0.1}_{-0.1}$
$(M/L)_{d,1}[M_\odot/L_\odot]$	$3.78^{+0.08}_{-0.09}$	$3.3^{+0.1}_{-0.1}$
$(M/L)_{d,2}[M_\odot/L_\odot]$	$1.17^{+0.06}_{-0.06}$	$0.81^{+0.1}_{-0.1}$
k_1	$0.42^{+0.01}_{-0.01}$	$0.44^{0.01}_{0.01}$
k_2	$0.53^{+0.01}_{-0.01}$	$0.53^{-0.01}_{+0.01}$

leads us to more robust results than purely photometric approaches. We are not focusing on any simple 'bulge+disc' decomposition here, instead, we are to propose a more general approach, as detailed starting from Section 4.

It is indeed possible for structures not directly modelled by BANG (such as bars, thick discs, etc.) to be mimicked by some combination of the structures actually included in the modelling (i.e. the bulge, the inner and outer discs). As an example, thick discs could possibly be modelled as the superposition of components 'D_1' and 'D_2' weighted with appropriate values of the kinematic decomposition parameters k_1 and k_2, while strongly non-axisymmetric components such as bars can only be modelled in their azimuth-averaged properties. We emphasize that even when the inner and outer discs are modelled as razor-thin exponential components, caution must be payed in interpreting them as dynamically cold thin discs. A physically motivated discussion cannot neglect considering their kinematic state.

4 ANALYSIS OF AN INDIVIDUAL GALAXY

In this section, we show the results of our analysis focusing on a specific galaxy. For this purpose we choose 1-256009 (MaNGA-ID) an S0a galaxy[6] exhibiting a regular rotation pattern at redshift $z = 0.04935$.

We fitted this galaxy, as we did for the whole sample, with three different models ('$B + D_1 + D_2$','$B + D_1$','$D_1 + D_2$') choosing the most statistically favoured according to the highest evidence criterion, '$B + D_1 + D_2$' in this case. We report in Table 2 the best-fitting parameters and their upper and lower errors[7] computed as the 50th, the 95th, and the 5th percentiles of the marginalized posterior distribution, both in the 'halo-fixed' and 'halo-free' configurations. The two models generally agree with a small scatter between most of the relevant parameters, especially regarding the stellar components. Given the limited spatial extension of the MaNGA kinematics, it is not clear whether and in which cases the halo parameters can be really constrained by the data, this is why, from now on, following a conservative approach, we will focus our analysis on the 'halo-fixed' configuration.[8]

Fig. 1 illustrates the best-fitting model obtained from our fit for the logarithm of the surface brightness (left-hand column), the line-of-sight velocity (middle column), and the line-of-sight velocity dispersion (right-hand column). The first and the second rows refer respectively to the data and the best-fitting model, while in the last row, we show the residuals respectively divided by the data errors: δB (for the brightness), δv (for the velocity), and $\delta\sigma$ (for the velocity dispersion). Comparing our model predictions with the data, we generally find a quite good agreement between all three quantities, as can be shown from the residual maps in the third row. In this case, the brightness differences between our model and the data (left-hand panel, third row) highlight the presence of a nuclear structure poorly fitted by our smooth and axially symmetric model.

In Fig. 2, we show the azimuthally average profiles of the brightness (left-hand panel), velocity (middle), and velocity dispersion (centre) for the full model (green line) showing a good agreement between our best-fitting model and the data (black dots).

We decided to decompose the galaxy into two more general components, dynamically hot and cold, respectively. Starting from the parameter of Table 2 we use the information about the originally assumed (bulge and discs) components to define the brightness profiles of the hot and cold constituents as:

$$B_{\rm hot}(r) = B_b(r) + (1-k_1)B_{d,1}(r) + (1-k_2)B_{d,2}(r), \tag{6}$$

and similarly for the cold component:

$$B_{\rm cold}(r) = k_1 B_{d,1}(r) + k_2 B_{d,2}(r). \tag{7}$$

We propose here a decomposition which accounts both for the geometrical structure of the galaxy constituents and for their kinematics state; keeping this in mind we include in the 'hot' component the bulge, which is entirely supported by dispersion, and a fraction of each disc in a way proportional to their degree of random motion.[9] As opposed, we define the 'cold' component as the disc brightness proportional to the rotation and hence proportional to k_1 and k_2.

Our decomposition can be visualized in the left-hand panel of Fig. 2 where we show the 'hot' and 'cold' brightness profiles, respectively in red and blue colours, as a function of the distance from the galaxy centre. The 'hot' component almost dominates in the whole physical region being, as expected, more important in the

[6]According to the MaNGA Visual Morphology Catalogue (VMC-VAC) (Vázquez-Mata et al. 2022)

[7]As already pointed out in Rigamonti et al. (2022b) most of the statistical errors are often smaller than a few percent; this is a quite common situation when using nested sampling algorithms, related to the simplified nature of the model not taking into account the whole underlying physics governing the problem at hand thus implicitly reducing possible degeneracies between parameters.

[8]Please refer to table 1 and appendix C for the discussion about the statistical consistency of the results obtained using the two different fitting procedures.

[9]Remember that the larger is $0 < k_{1;2} < 1$ the more is the rotational motion of the disc, thus implying that $1 - k_{1;2}$ is proportional to the dispersion support.

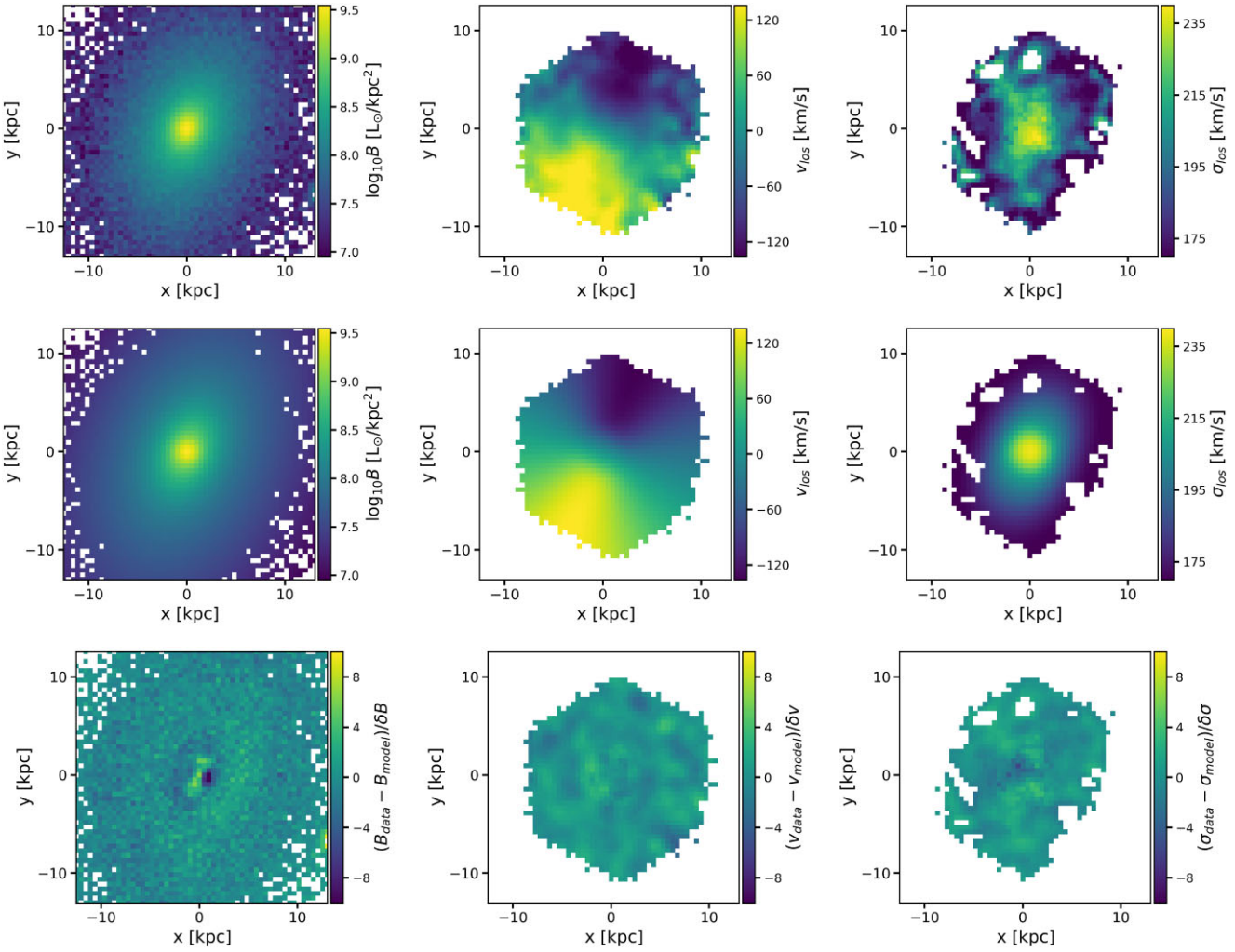

Figure 1. Best-fitting model of the 8258–6102 galaxy. The first, second, and third columns refer to the surface brightness, the line-of-sight velocity and the line-of-sight velocity dispersion, respectively. From top to bottom we report the observational data, the best-fitting model, and the residual maps. The residuals are computed as differences between the data and the model divided by the data errors δB δv, $\delta \sigma$.

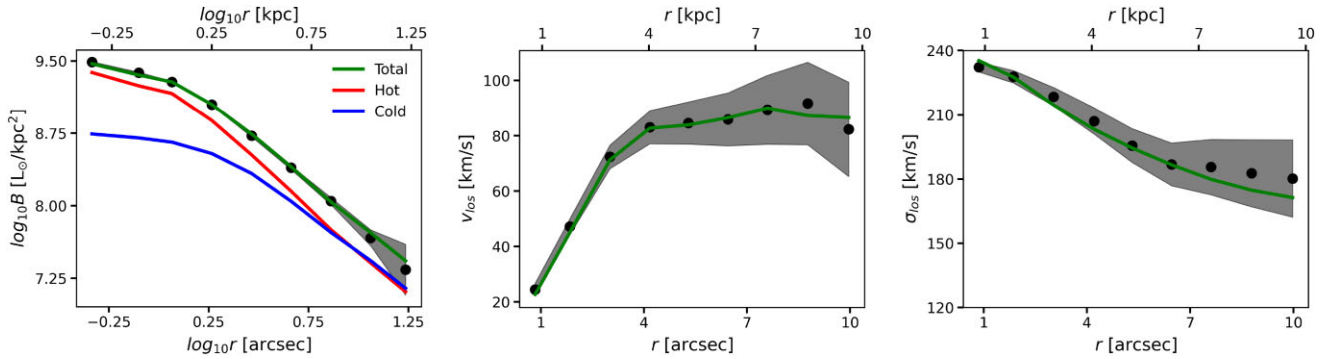

Figure 2. Average radial profiles of the logarithm of the surface brightness (left-hand panel), of the velocity (middle panel), and of the line-of-sight velocity dispersion (right-hand panel). The data are reported as black dots, with the errors, computed by an azimuthal average, shown as a grey-shaded area. The green lines refer to the best-fitting model, while the red and blue lines refer to a kinematic decomposition of the galaxy in its dispersion-dominated and rotation-dominated components (we refer to Sec. 4 for further details on this tentative decomposition).

Table 3. Table summary of decomposition adopted in par. 4 for the 1–256009 galaxy reporting total stellar masses and half-mass radii of each component together with their light and mass fraction in respect to the whole galaxy and within the R_e. The first two columns are the description of the parameter together with the associated name while the third column refers to the best-fitting value and the errors, estimated as in Table 2.

Description	Name	Value
Total stellar mass	$\log_{10}(M_\star/\mathrm{M}_\odot)$	$11.27^{+0.01}_{-0.01}$
Total hot mass	$\log_{10}(M_{\rm hot}/\mathrm{M}_\odot)$	$11.09^{+0.01}_{-0.01}$
Total cold mass	$\log_{10}(M_{\rm cold}/\mathrm{M}_\odot)$	$10.81^{+0.01}_{-0.01}$
Half-mass radius	$\log_{10}(R_{\rm half,\star}/\mathrm{kpc})$	$0.50^{+0.01}_{-0.01}$
Half-mass radius hot component	$\log_{10}(R_{\rm half,hot}/\mathrm{kpc})$	$0.33^{+0.01}_{-0.01}$
Half-mass radius cold component	$\log_{10}(R_{\rm half,cold}/\mathrm{kpc})$	$0.75^{+0.02}_{-0.02}$
Hot ratio (mass)	$M_{\rm hot}/M_\star$	$0.65^{+0.01}_{-0.01}$
Cold ratio (mass)	$M_{\rm cold}/M_\star$	$0.35^{+0.01}_{-0.01}$
Hot ratio (light)	$L_{\rm hot}/L_\star$	$0.60^{+0.01}_{-0.01}$
Cold ratio (light)	$L_{\rm cold}/L_\star$	$0.40^{+0.01}_{-0.01}$
Hot ratio within R_e (mass)	$M_{\rm hot}(R_e)/M_\star(R_e)$	$0.73^{+0.01}_{-0.01}$
Cold ratio within R_e (mass)	$M_{\rm cold}(R_e)/M_\star(R_e)$	$0.27^{+0.01}_{-0.01}$
Hot ratio within R_e (light)	$L_{\rm hot}(R_e)/L_\star(R_e)$	$0.71^{+0.01}_{-0.01}$
Cold ratio within R_e (light)	$L_{\rm cold}(R_e)/L_\star(R_e)$	$0.29^{+0.01}_{-0.01}$

centre; we note that the two discs, given their mild rotation ($k_1 = 0.42$ and $k_2 = 0.53$), add a relevant contribution to the 'hot' component.

We report in Table 3 masses and half-mass radii of the 'hot' and 'cold' decomposition together with their fraction for the whole galaxy and within the effective radius (R_e). We refer to Section 5 for further discussion about any biases and limitations about our definition of 'hot' and 'cold' components.

5 COMPARISON WITH PREVIOUS DYNAMICAL MODELLING ESTIMATES

In this section, we compare our results for the same subsample of 149 early-type galaxies (ETGs) analysed by Jin et al. (2020) with a Schwarzschild orbit superposition method (Schwarzschild 1979; van den Bosch et al. 2008; Jethwa et al. 2020).[10]

Orbit-based methods represent the state-of-the-art dynamical modelling techniques allowing deep investigation of the internal structure of galaxies, fully characterizing their phase-space distribution and thus offering an optimal benchmark for comparison.

Despite the robustness of these modelling techniques, their applicability, mainly due to the large computational cost, has been limited to a few hundred galaxies. BANG can offer an alternative and also a complementary approach to the problem of galactic dynamical modelling, especially in cases of large data samples. We, therefore, test our approach against such reliable modelling techniques to prove and check the robustness of our modelling.

In the left-hand panel of Fig. 3, we compare stellar mass predictions, again as twice the mass within the effective radius. The agreement is good in the whole range of masses with an average scatter, computed as the standard deviation of the differences, of $\simeq 0.07$ dex, corresponding to a mean relative error of $\simeq 6$ per cent. Only one outlier is evident, identified in 8263–9102 (green diamond on the plots), an elliptical galaxy clearly showing a twisting of the rotation pattern implying a geometrical structure far from axial symmetry and, hence, not consistent with BANG's modelling assumptions. Given the rarity of those examples in the MaNGA data set, we expect our analysis not to suffer from any biases arising from those peculiar cases (Jin et al. 2016; Feng et al. 2022).

In the middle and right-hand panels of Fig. 3 we show a comparison between our tentative 'hot' versus 'cold' decomposition (horizontal axis) and the orbital analysis extrapolated from Schwarzschild modelling (Jin et al. 2020, vertical axis). Finding a way to compare the two analyses is not straightforward. Jin et al. (2020) orbital decomposition is luminosity-weighted and limited to R_e. We therefore computed our 'hot', 'cold', and 'total' luminosity as:

$$L_{\rm hot}(R_e) = \frac{M_b(R_e)}{(M/L)_b} + (1-k_1)\frac{M_{d,1}(R_e)}{(M/L)_{d,1}} + (1-k_2)\frac{M_{d,2}(R_e)}{(M/L)_{d,2}}, \quad (8)$$

$$L_{\rm cold}(R_e) = k_1\frac{M_{d,1}(R_e)}{(M/L)_{d,1}} + k_2\frac{M_{d,2}(R_e)}{(M/L)_{d,2}}, \quad (9)$$

$$L_\star(R_e) = \frac{M_b(R_e)}{(M/L)_b} + \frac{M_{d,1}(R_e)}{(M/L)_{d,1}} + \frac{M_{d,2}(R_e)}{(M/L)_{d,2}}, \quad (10)$$

where $M_j(R_e)$ with ($j = \{b; d, 1; d, 2\}$) is the enclosed mass of the j-th component within R_e. Moreover, we compared our 'hot' fraction with the sum of 'hot' and 'counter-rotating' orbits since those are the ones expected to have the largest contribution to dispersion; similarly, most of the rotational support (our 'cold' fraction) should reside in both 'warm' and 'cold' orbits. We highlight that the counter-rotating fraction decreases only by a slight amount the scatter in the middle panel of Fig. 3, acting more as a systematic shift and indicating almost no correlation with $L_{\rm hot}(R_e)/L_\star(R_e)$. Similarly, in these galaxies, $f_{\rm cold}$ is generally small, making it difficult to quantify whether $L_{\rm cold}(R_e)/L_\star(R_e)$ is more a proxy of the 'warm' or 'cold' orbital families.

The two pictures show a correlation in the 'hot' and the 'cold' cases,[11] even though the scatter is quite relevant ($\simeq 0.12$) given the limited dynamic range. A systematic offset ($\simeq 0.12$) is present in both the 'hot' and 'cold' fractions mainly due to intrinsic differences in the two approaches; we account for a decomposition proportional to k_1 and k_2, meaning that even when they are large enough (i.e. $k_{1,2} \gtrsim 0.8$) to suggest the presence of a dynamically cold disc, still a non-negligible amount of the galaxy mass will be added to the hot component possibly resulting in an overestimation of its contribution. Differently, in Schwarzschild-based approaches, orbits are divided into families depending on constant circularity thresholds thus assigning, in the example of a dynamically cold disc, all of the mass to the cold component. Note that the offset between the hot (cold) fraction predicted by DYNAMITE analysis on simulated galaxies shown in Jin et al. (2019) is consistent (but opposite in sign) to the offset of our decomposition with respect to DYNAMITE shown in the middle (right-hand) panel of Fig. 3. This may suggest that the main source of disagreement between DYNAMITE and BANG could be due to an underestimate of hot orbits in DYNAMITE and not necessarily to an overestimate in BANG. A more quantitative analysis of the differences between the two approaches is beyond the scope of this paper.

[10]Note that the work presented in Jin et al. (2020) has been completed before the discovery of a minor and statistically irrelevant bug in the orbit mirroring scheme present in their implementation (Thater et al. 2022).

[11]Note that our definitions of 'hot' and 'cold' components are complementary to each other so that a relationship seen with one of the two quantities is present also with the other by construction.

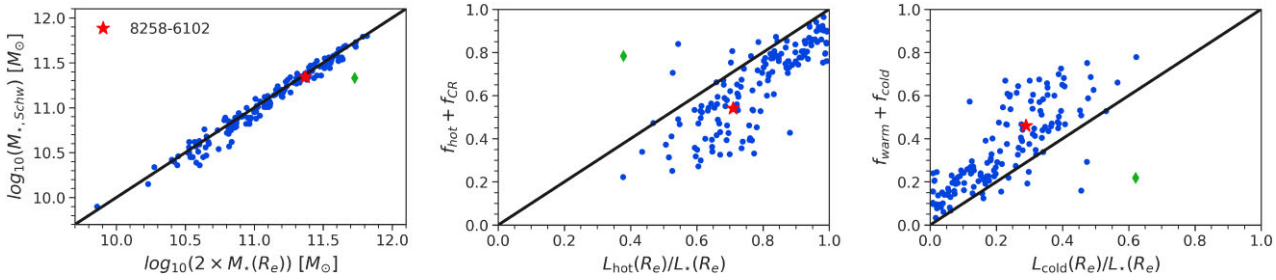

Figure 3. Comparison between our estimates and predictions from the Schwarzschild orbit superposition method on the 149 galaxies analysed in Jin et al. (2020). From left to right we compare our estimates (on the x-axis) of stellar mass, hot, and cold luminosity weighted fractions, respectively, with the stellar mass, 'hot'+'counter-rotating' orbital fractions and 'warm' + 'cold' orbital fractions presented in Jin et al. (2020). The stellar masses are estimated as twice the mass at the effective radius (R_e) while our hot and cold fractions are estimated from equations (8), (9), and (10). The red star refers to the galaxy presented in 4 (i.e. 8258–6102), the blue dots refer to the other 148 galaxies while the black line shows the one-to-one relation.

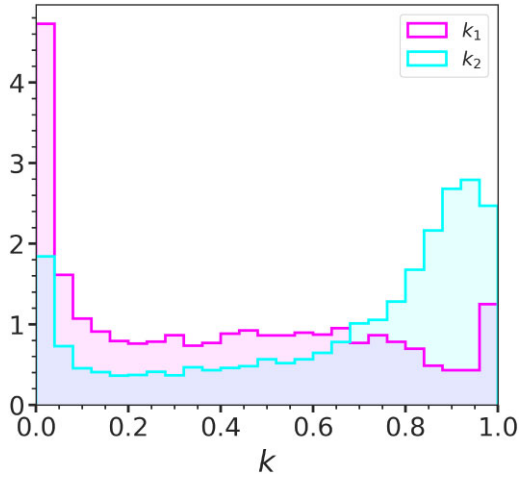

Figure 4. Distribution of the kinematic decomposition parameters of the inner (k_1) and outer (k_2) discs, respectively, in magenta and cyan. Each histogram is normalized such that the total area sums to one.

6 PRELIMINARY ANALYSIS ON THE PROPOSED DECOMPOSITION

In this section, we present some of the results obtained from our analysis focusing mainly on the hot-cold decomposition proposed in the previous paragraphs and characterizing it in terms of visual morphology and kinematics. We show here the results of our analysis performed over the whole MaNGA sample comprising, as reported in Section 3, 10 005 galaxies roughly composed by 62 per cent of spirals, 21 per cent of lenticulars, and 17 per cent of ellipticals[12] with a best fit corresponding to a 'B + D_1 + D_2', 'B + D_1' a 'D_1 + D_2' model respectively in $\simeq$ 86 per cent, $\simeq$ 6 per cent, and $\simeq$ 8 per cent of the cases. Unless otherwise specified, all the forthcoming analysis is performed on such sample, which we refer to as the 'main sample'. We moreover refer to Appendix B for the same analysis on a selected subsample.

Fig. 4 shows the distributions of the kinematic decomposition parameters k_1 and k_2 for the inner and the outer discs. The inner disc has a significant peak for low values of k_1, indicating the presence of dispersion-supported exponential structures in galaxy internal regions; we argue that those discs account for corrections to the classical bulge, assumed to be perfectly spherical in our modelling. A relevant number of galaxies show intermediate rotational support spanning a wide range of k_1, probably indicating the presence of a variety of more or less rotating structures in galaxy centres.

As expected, the outer disc shows a clear peak at high values of k_2 (i.e. $k_2 \simeq 0.9$) tracing, in these cases, the rotationally supported component of the galaxy. Another peak is present in the dispersion-dominated domain (i.e. $k_2 \lesssim 0.15$); interpreting those components as thin discs may be misleading since the majority of galaxies contributing to this are massive ellipticals dominated by dispersion. Given their not-always-spherical light distribution and the absence of ordered rotation, we model these systems as a superposition of dispersion-supported exponential 'discs'.

It is clear by this discussion that analysing bulges and discs, as defined by BANG, without accounting for their kinematic state may lead to biased and incorrect conclusions; this is why we focus the following analysis on what we previously defined as 'hot' and 'cold' components (see Section 5):

$$M_{\rm hot} = M_b + (1 - k_1)M_{d,1} + (1 - k_2)M_{d,2}, \tag{11}$$

$$M_{\rm cold} = k_1 M_{d,1} + k_2 M_{d,2}, \tag{12}$$

where $M_{\rm hot}$ and $M_{\rm cold}$ are, respectively, the mass of the 'hot' and 'cold' component.

Fig. 5 shows the distribution of masses, respectively, for the 'hot' (left-hand panel) and 'cold' (middle) components together with the total stellar mass (right-hand panel) of the galaxy colour-coded by visual morphology (spirals in blue, lenticulars in green, and ellipticals in red). Focusing on the first panel, we can notice, as expected, a clear trend between the 'hot' mass and the morphology with elliptical galaxies skewed at the high-mass end of the distribution; lenticulars and spirals are, on average, less massive with a broader distribution and contributing in the whole dynamical range.[13] On the top panel of the picture, we show the distribution for the whole sample demonstrating that, even though ellipticals dominate in terms of mass, their number, in the analysed sample, is less significant; we stress that these histograms are affected by the selections criteria adopted in the MaNGA survey and cannot be considered (without accounting for the proper corrections) representative of the real local galaxy population (Wake et al. 2017).

Similar trends can be seen in the $M_{\rm cold}$ distribution. Ellipticals are still skewed at high masses peaking much closer to lenticulars. For both lenticulars and spirals the distributions span very similar ranges

[12] According to the VMC-VAC Vázquez-Mata et al. (2022)

[13] As we show in appendix B even applying some quality cuts on the sample, the general trends between the different distributions are unaffected.

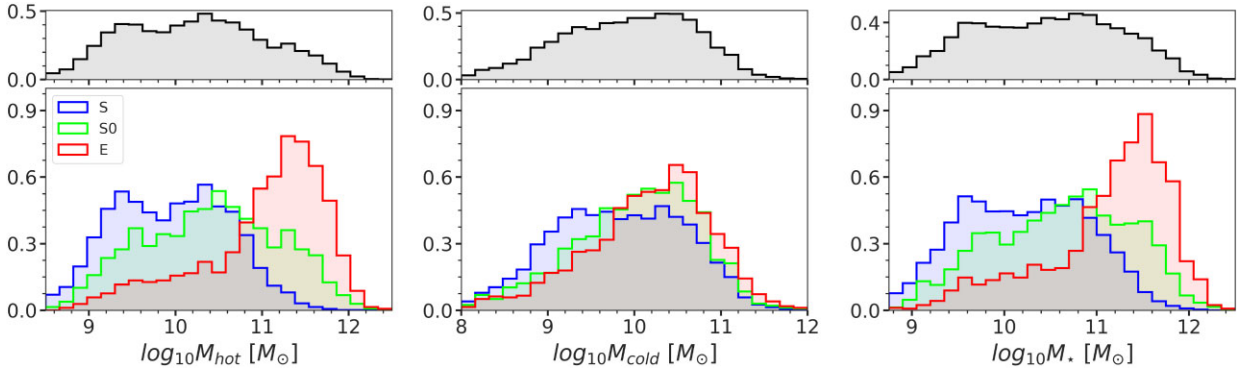

Figure 5. From left to right we show the mass distribution of the hot, cold, and total stellar mass for the sample under analysis. The hot and cold mass is estimated following equations (11) and (12). Each histogram is normalized to have a total area equal to one, and the distributions are colour coded according to visual morphology: blue for spirals, green for lenticulars, and red for ellipticals. The panel over each picture represents the distribution of that variable for the whole population helping in understanding the relative role of the three morphological types.

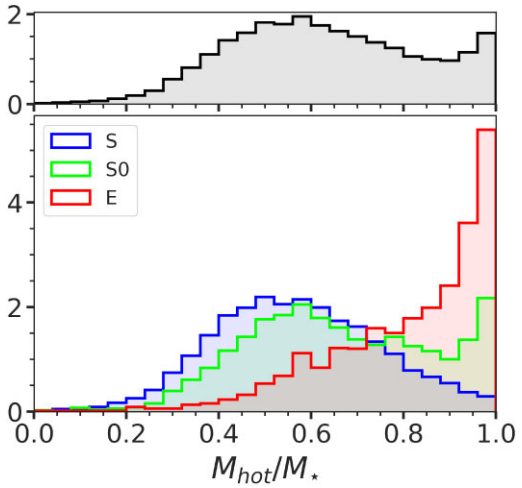

Figure 6. Distribution of the 'hot' (see equation 11) over total stellar mass fraction colour-coded according to morphology: blue for spirals, green for lenticulars, and red for ellipticals. Each histogram is normalized to have a total area equal to one. The top panel shows in black and grey the distribution for the whole sample.

compared to their 'hot' counterparts suggesting an increase in the rotational support (if compared to ellipticals) with a still relevant contribution from dispersion-dominated structures.

The last panel on the right shows the distribution of the total stellar mass for each galaxy mostly reflecting the behaviour of the 'hot' ('cold') component in the high (low) mass bins, stressing their role and their dependence on stellar mass in the overall galaxy budget. We verified that our stellar masses are consistent with the prediction from the NASA-Sloan Atlas (NSA)[14] settling on linear relation with a small offset of 0.04 dex and a scatter of 25 km s^{-1}.

This is even clearer if we look at Fig. 6 showing the fraction between the 'hot' and total mass of the galaxy colour-coded in the same way as done in Fig. 6. As expected, the 'hot' component largely dominates in the case of ellipticals. Interestingly, lenticulars demonstrate a bimodal distribution; a fraction of them, peaking at $M_{\rm hot}/M_\star \simeq 1.0$, is entirely supported by dispersion and further inspection is needed to address if these objects may have misclassified visual morphology according to the VMC-VAC (Vázquez-Mata et al. 2022). Spiral galaxies have, in terms of mass, a considerable contribution from the hot component with a broad distribution skewed towards high values of $M_{\rm hot}/M_\star$. Even though this could be surprising, we stress again that our definition of the 'hot' component always includes a fraction of the disc mass even in cases of rotationally supported systems. We note also that a large contribution to the hot component mass of spirals comes from the two discs (second and third terms of equation 11), possibly indicating that a simple spherical bulge cannot account for the variety of inner galactic structures (such as bars etc...) that are often present in spiral and that can be a relevant source of dispersion. The distribution of ellipticals shows a prominent tail towards small values of $M_{\rm hot}/M_\star$ possibly suggesting that visual morphology alone cannot always be reliable while characterizing the kinematic state of a galaxy (Krajnović et al. 2008; Cappellari et al. 2011).

[14] http://nsatlas.org/

7 SCALING RELATIONS IN THE WHOLE MANGA SAMPLE

Correlations between photometric and kinematic properties have been extensively studied for investigating the matter content of galaxies. As first attempts, scaling relations between the total stellar or baryonic matter with the maximum circular velocity (or a proxy of it) have been discovered for late-type galaxies (LTGs; Tully & Fisher 1977). Similarly, in the case of ETGs, a correlation exists between stellar mass and stellar velocity dispersion (Faber & Jackson 1976) as a projection of the more general fundamental plane relation (Djorgovski & Davis 1987; Dressler et al. 1987) which, at first order, can be interpreted as a consequence of the virial theorem.

All these relations demonstrate the implicit connection, through the Poisson equation, between the distribution of mass (or density) and the stellar kinematic (or the gravitational potential). This is why, aiming at unifying ETGs and LTGs on the same scaling law, a new correlation, combining rotational and random motion, has been recently proposed (Weiner et al. 2006).

In the following, we do not aim at any detailed study regarding scaling relations. Given their universality, we instead use them as a validating tool for our modelling scheme, probing the ability of BANG in recovering the stellar mass and the gravitational potential, and its

robustness against outliers (such as mergers, non-masked stars, and type I AGNs or other contaminants).

For consistency with previous works (Cortese et al. 2014; Aquino-Ortíz et al. 2018, 2020) and to show the generalization ability of our modelling scheme and its robustness against outliers together with the results on the main sample (see Section 6) we repeated the analysis on a carefully selected subsample of galaxies selected according to the same criteria adopted in Aquino-Ortíz et al. (2020). More specifically, in the latter case, we considered only galaxies with an inclination angle $25 < i < 75$, masking all the pixels with an error in the velocity larger than 25 km s^{-1} ($\simeq$ 1/3 of the average MaNGA spectral resolution $\sigma_{inst} \simeq 70$ km/s), and discarding all galaxies with more than 40 per cent pixels masked within an ellipse of semimajor axis equal to the effective radius of the galaxy. As a final cut, we visually inspected all the objects in our sample excluding ongoing mergers or other contaminants (i.e. wrong redshift, central non-masked stars, and type I AGNs); in the following we refer to this sample as 'kinematic sample'

We focus our analysis on the scaling relation proposed in Weiner et al. (2006) relating the stellar rotational and dispersion support within R_e to the enclosed stellar mass of the galaxy ($M_\star(R_e)$).

The left-hand panel of Fig. 7 shows the relation between $M_\star(R_e)$ (y-axis) and V_{R_e} colour-coded by visual morphology. $M_\star(R_e)$ is the stellar mass within the effective radius and it is computed from the best-fitting stellar mass profile as predicted by BANG, while V_{R_e} is a proxy of the rotation velocity within the effective radius estimated following Aquino-Ortíz et al. (2020). More specifically, starting from the l.o.s. velocity maps as modelled by BANG, we considered all the pixels within an ellipse of semimajor axis equal to the effective radius of the galaxy and we estimated V_{Re} by computing the difference between the 90th and 10th percentile (i.e. $W = (V_{90} - V_{10})/2$) of its velocity histogram and accounting for deprojection by dividing for $\sin i$, being i the inclination angle estimated by BANG. As expected, a linear correlation is present in the case of spirals, even though the scatter is significant and it largely increases changing morphology, with ellipticals dominating the spread in V_{R_e} mainly due to the huge contribution of slow rotators.

Due to the morphology dependence of this relation, following several works in the literature, we define:

$$S_{\rm K}(R_e) = \sqrt{K\ V_{R_e}^2 + \sigma_{R_e}^2}, \tag{13}$$

where σ_{R_e} is the average velocity dispersion within R_e and the constant multiplicative factor K is usually set equal to 0.5 (Cortese et al. 2014; Aquino-Ortíz et al. 2018; Barat et al. 2019; Gilhuly, Courteau & Sánchez 2019). We estimate σ_{R_e} starting from l.o.s. velocity dispersion best-fitting model and linearly averaging over the same elliptical region as defined above. We estimated the errors on $M_\star(R_e)$, V_{R_e}, and σ_{R_e} by repeating the procedure detailed above, with the model parameters associated with the 15 and 85 percentile of the posterior distribution.[15]

In all cases, we fitted a line to the data points by considering errors on both the x and y axes. Doing that would generally require a fit with at least $N + 3$ free parameters (where N is the number of considered data points, see Andreon & Hurn 2013), an impractical solution in our case. Luckily, in the case of a straight line, it is still possible to reduce the parameter space dimension back to three (slope, intercept, and optionally, intrinsic scatter) under a few simplifying assumptions (see chapter seven of Hogg, Bovy & Lang 2010 for further details).

Following Aquino-Ortíz et al. (2020), we considered the stellar mass as the independent variable fitting, with CPNEST (Veitch et al. 2017), the following functional form:

$$\log_{10}\left(\frac{S_{0.5}(R_e)}{100\ {\rm km\ s^{-1}}}\right) = a + b\log_{10}\left(\frac{M_\star(R_e)}{10^{10.5}\ {\rm M_\odot}}\right), \tag{14}$$

where a and b are, respectively, the intercept and the slope of the relation and together with the intrinsic scatter σ are the free parameters of the fit.

The $M_\star(R_e) - S_{0.5}(R_e)$ is presented in the middle panel (Fig. 7); the additional contribution of the dispersion component helps in reducing the scatter moving all galaxies on a similar linear relation. The best-fitting results on the whole sample are presented in the first line of Table 4, with an exceptional agreement, in terms of the slope,[16] with what found in Aquino-Ortíz et al. (2020). This result is even more striking considering that we see a significant reduction (about 30 per cent less if compared to sample and analysis of 2458 galaxies presented in Aquino-Ortíz et al. 2020) of the scatter in the relation, even though our sample comprises $\simeq$ 10 000 galaxies, demonstrating the ability of BANG of recovering the true gravitational potential of galaxies and its robustness against outliers, strengthening our results, and motivating its blind applicability even on larger samples.

Driven by these results, we provide in the third panel of the figure a new kinematic tracer computed by dividing V_{R_e} with a proxy of the average rotational support of the galaxy (k_{R_e}). Similarly to what was done in Rigamonti et al. (2022b), we compute k_{R_e} for each galaxy as the brightness-weighted average of the k_1 and k_2 parameters within R_e. Note k_{R_e} is limited between zero and one resulting in major corrections for slowly rotating galaxies. We provide through the following functional form an empirical relation for estimating k_{R_e} directly from V_{R_e}/σ_{R_e}:

$$k_{R_e} = 1 + \frac{\operatorname{arccot}\left[b\left(V_{R_e}/\sigma_{R_e} - x_0\right)\right]}{\arctan(bx_0) + \pi/2}, \tag{15}$$

where $b = 1.47$ and $x_0 = 0.086$ are calibrated by fitting that profile on our estimates obtained from the MaNGA sample. Note that equation (15) ensures that k_{R_e} is equal to zero (one) for $V_{R_e}/\sigma_{R_e} = 0$ (∞). Fig. 8 shows the relation between k_{R_e} and V_{R_e}/σ_{R_e} colour coded according morphology. As expected, spiral galaxies (blue dots) are supported by rotation, while ellipticals dominate the dispersion regime.

Fitting the following linear relation:

$$\log_{10}\left(\frac{V_{R_e}/k_{R_e}}{100\ {\rm km\ s^{-1}}}\right) = a + b\log_{10}\left(\frac{M_\star(R_e)}{10^{10.5}\ {\rm M_\odot}}\right), \tag{16}$$

to the proposed correction gives the same results, in terms of the slope, as the $M_\star(R_e) - S_{0.5}(R_e)$ relation, reducing, even more, the scatter and possibly suggesting V_{R_e}/k_{R_e} as being a better indicator of the relation between stellar mass and the underlying gravitational

[15] A proper Bayesian approach would require to evaluate our model on the whole posterior distribution estimating the best fit and its error by computing the median and the percentiles on the actual set of models instead of the parameter posteriors. For computational reasons, we refrain from following this strategy; this is why we opted for what is discussed in the text.

[16] A comparison of the zero point of the relation with literature results is not trivial due to possible differences in the mass estimates and the sample selection.

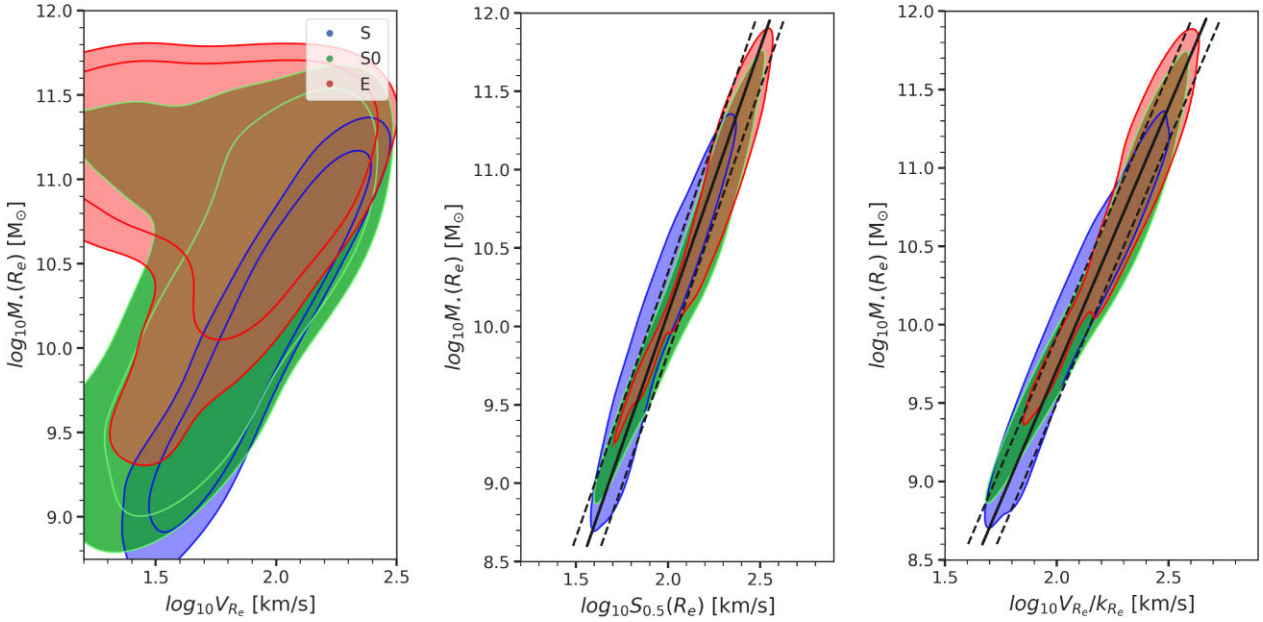

Figure 7. Scaling relations of different kinematics tracers divided according to morphology (blue for spirals, green for lenticulars, and red for ellipticals). In all three plots, the y-axis is the logarithm of the stellar mass within one R_e, while the horizontal axis, respectively from left to right, shows the logarithm of the velocity at one R_e (V_{R_e}), the logarithm of the $S_{0.5}$ parameter (see equation 13) and the logarithm of the velocity at R_e corrected according to equation (15). For each morphological class, the coloured area contains 80 per cent of the kernel density estimated probability mass, only for the first plot on the left we included a second contour at a 70 per cent level. The solid black lines are the best-fitting linear relations while the black dotted lines represent the one$-\sigma$ confidence interval. The best-fitting parameters are summarized in Table 4.

Table 4. Summary table of the best-fitting parameters for the linear fit (equations 14, 16) of the kinematic tracers presented in the middle and left-hand panels of Fig. 7. The first column refers to the considered dependent variable (the independent variable is always $M_\star(R_e)$), while the other three columns are the free parameters of the fit, namely, the intercept (a), the slope (b) and the intrinsic scatter σ.

y-axis	a	b	σ
$\log_{10}S_{0.5}(R_e)$	0.13 ± 0.01	0.30 ± 0.01	0.073
$\log_{10} V_{R_e}/k_{R_e}$	0.24 ± 0.01	0.30 ± 0.01	0.064

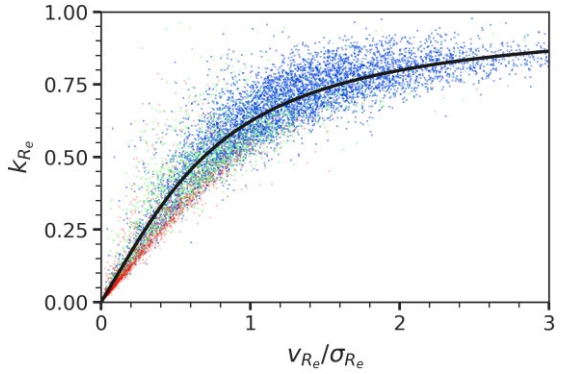

Figure 8. On the x-axis velocity at the effective radius divided by average velocity dispersion; on the y-axis the luminosity weighted average rotational support at R_e. Points are colour coded in the same way as done in Fig. 7. The black solid line is the best fit to the data of the functional form presented in equation (15).

Table 5. Same as Table 4 but for 'kinematic sample' ($\simeq$ 7000 galaxies) selected according to the same criteria applied in Aquino-Ortíz et al. (2020) and defined at the beginning of Section 7.

y-axis	a	b	σ
$\log_{10}S_{0.5}(R_e)$	0.13 ± 0.01	0.31 ± 0.01	0.065
$\log_{10} V_{R_e}/k_{R_e}$	0.24 ± 0.01	0.31 ± 0.01	0.053

potential.[17] Note that with the provided correction the scatter in the linear relation becomes almost consistent with the scatter in the Tully–Fisher relation for pruned samples (Lelli et al. 2019).

For both kinematic tracers ($S_{0.5}(R_e)$ and V_{R_e}/k_{R_e}) the results of a linear fit are still consistent with each other even when repeating the analysis on the 'kinematic sample' defined in the first part of Section 7, with a further decrease in the scatter of the relation (Table 5). We speculate that a possible bending may be present in those relations (see Appendix A) since a fit with two lines gives a larger evidence than with a single one; this may hint at a decrease of the M_{star}/M_h fraction in the high stellar mass end (Noordermeer & Verheijen 2007; Moster, Naab & White 2018; Behroozi et al. 2019). Further analysis is still required before drawing any conclusion, especially given the priors assumed on the halo.

8 SUMMARY AND CONCLUSIONS

In this work, we presented some results from the application of BANG, a software purposely designed for bulge+discs dynamical

[17]Note that we use k_{R_e} as estimated from equation (15) and not directly from BANG, thus the reduction of the scatter in the last panel of Fig. 7 may be also driven by that.

modelling of galaxies, on the galaxies observed by the MaNGA survey. Being fast (GPU-based) and coupled with robust Bayesian parameter estimation techniques (e.g. Nested Sampling), BANG is perfectly suited for automated applications to large galaxy data sets. We improved upon the earlier version of BANG discussed in Paper I both in the modelling approach and, by accounting for physically motivated priors, in the parameter estimation set-up.

We successfully modelled the photometry and kinematic of 10 005 galaxies assuming three different possible configurations (i.e. bulge+inner disc+outer disc, bulge+inner disc, inner disc+outer disc) with two different halo prior assumptions,[18] estimating the structural and dynamical parameters for each galaxy of the sample (see Table 1 for a summary of the free parameters in the models).

In order to test the accuracy of the methodology, we compared our results to well-known kinematic scaling relations (e.g. $M_\star$ versus $S_{0.5}$; Weiner et al. 2006), finding a substantial agreement (regardless of the assumed halo prior) with previous works in the literature, for all kind of morphologies (see e.g. Aquino-Ortíz et al. 2020). We also provide an empirical correction, dependent on the velocity-to-dispersion ratio, able to reduce the scatter in the stellar mass-to-velocity relation, resulting in a tighter correlation when compared to the $M_\star(R_e)$ versus $S_{0.5}$. These results do not assume any particular selection criteria and highlight the power of BANG in recovering the gravitational potential of single galaxies even in an automated decomposition applied to large samples.

We also compared stellar mass estimates for a subsample of 149 ETGs galaxies analysed through Schwarzschild orbit superposition methods (Jin et al. 2020), finding an excellent agreement. We therefore propose a new decomposition scheme that combines the visible components of our model (i.e. bulge, inner disc, and outer disc) into more general, and dynamically motivated, 'hot' and 'cold' components. This decomposition correlates with purely orbit-based estimates, possibly helping in extending studies of the 'hot' versus 'cold' mass budget to larger samples.

We performed a preliminary analysis of the distribution of the structural components for different morphological types. We showed that the physical interpretation of the two exponential disc components of the model depends on their kinematical parameters k_1 and k_2. In cases where k_1 is small, the inner disc typically models a non-spherical central structure dominated by dispersion. Similarly, when k_2 is small, the outer disc (potentially in conjunction with the inner disc) models non-circular isophotes in ellipticals. The detailed analysis of the possible many real natures of the two discs is deferred to an ongoing investigation. As expected, our definition of 'hot' and 'cold' mass correlates with the morphological type, with ellipticals and spirals positioned at the high and low ends, respectively, of the 'hot' fraction distribution.

Our work aimed to demonstrate the proposed methodology's ability to cope with large samples and to validate our results. The preliminary analysis presented in Section 6 paves the road to further developments which we will address in future works. In particular, we will exploit our parametrization k_1 and k_2 to clarify the role that the two discs have in determining the dynamic state of the internal components of galaxies. We will quantify the mass budget of each component also in dependence on the star-formation rate of the galaxy. This will help us to understand the relative role of mergers versus coherent accretion in shaping local galaxies (Rigamonti et al., to be submitted). We also plan to characterize the possible rotational support of photometric bulges, hence breaking the degeneracy between classical bulges and pseudo-bulges. We also aim at applying BANG to mock simulation-based catalogues (e.g. iMaNGA; Nanni et al. 2022) in order to select the parameter space region that could identify and characterize thick discs and, possibly, bars.

[18] for a grand total of +60 000 different fits.

ACKNOWLEDGEMENTS

We thank the anonymous referee for their comments and suggestions that helped us to improve the quality of the paper.

We gratefully thank Francesco Bollati, Stefano Zibetti, Matteo Fossati, and Walter Del Pozzo for the many insightful and constructive discussions that improved the quality of this work. FH and MD acknowledge funding from MIUR under the grant PRIN 2017-MB8AEZ. MD acknowledges financial support from ICSC – Centro Nazionale di Ricerca in High-Performance Computing, Big Data and Quantum Computing, funded by European Union – NextGeneration EU. LC acknowledges support from the Australian Research Council Future Fellowship and Discovery Project funding scheme (FT180100066,DP210100337). Parts of this research were conducted by the Australian Research Council Centre of Excellence for All Sky Astrophysics in 3 Dimensions (ASTRO 3D), through project number CE170100013.

DATA AVAILABILITY

The data underlying this article will be shared on reasonable request to the corresponding author. The full data base will be publicly available in a forthcoming paper (Rigamonti et al., to be submitted).

REFERENCES

Abdurro'uf et al., 2022, ApJS, 259, 35
Andreon S., Hurn M., 2013, Stat. Anal. Data Min., 6, 15
Aquino-Ortíz E. et al., 2018, MNRAS, 479, 2133
Aquino-Ortíz E. et al., 2020, ApJ, 900, 109
Barat D. et al., 2019, MNRAS, 487, 2924
Behroozi P., Wechsler R. H., Hearin A. P., Conroy C., 2019, MNRAS, 488, 3143
Belfiore F. et al., 2019, AJ, 158, 160
Bertin E., Mellier Y., Radovich M., Missonnier G., Didelon P., Morin B., 2002, in Bohlender D. A., Durand D., Handley T. H.eds, ASP Conf. Ser. Vol. 281, Astronomical Data Analysis Software and Systems XI. Astron. Soc. Pac., San Francisco, p. 228
Blanton M. R., Kazin E., Muna D., Weaver B. A., Price-Whelan A., 2011, AJ, 142, 31
Blanton M. R. et al., 2017, AJ, 154, 28
Bundy K. et al., 2015, ApJ, 798, 7
Cappellari M. et al., 2011, MNRAS, 416, 1680
Cappellari M. et al., 2013, MNRAS, 432, 1709
Cherinka B. et al., 2019, AJ, 158, 74
Cortese L. et al., 2014, ApJ, 795, L37
de Souza R. E., Gadotti D. A., dos Anjos S., 2004, ApJS, 153, 411
De Vaucouleurs G., 1948, Ann. Astrophys., 11, 247
Dehnen W., 1993, MNRAS, 265, 250
Djorgovski S., Davis M., 1987, ApJ, 313, 59
Dressler A., Lynden-Bell D., Burstein D., Davies R. L., Faber S. M., Terlevich R., Wegner G., 1987, ApJ, 313, 42
Drory N. et al., 2015, AJ, 149, 77
Dutton A. A., Macciò A. V., 2014, MNRAS, 441, 3359
Erwin P. et al., 2015, MNRAS, 446, 4039
Faber S. M., Jackson R. E., 1976, ApJ, 204, 668
Feng S., Shen S.-Y., Yuan F.-T., Dai Y. S., Masters K. L., 2022, ApJS, 262, 6
Freeman K. C., 1970, ApJ, 160, 811

Gavazzi G., Franzetti P., Scodeggio M., Boselli A., Pierini D., 2000, A&A, 361, 863
Gilhuly C., Courteau S., Sánchez S. F., 2019, MNRAS, 482, 1427
Hogg D. W., Bovy J., Lang D., 2010, preprint (arXiv:1008.4686)
Jethwa P., Thater S., Maindl T., Van de Ven G., 2020, DYNAMITE: DYnamics, Age and Metallicity Indicators Tracing Evolution, record ascl:2011.007
Jin Y. et al., 2016, MNRAS, 463, 913
Jin Y., Zhu L., Long R. J., Mao S., Xu D., Li H., van de Ven G., 2019, MNRAS, 486, 4753
Jin Y., Zhu L., Long R. J., Mao S., Wang L., van de Ven G., 2020, MNRAS, 491, 1690
Kormendy J., Kennicutt R. C., 2004, Annu. Rev. Astron. Astrophys., 42, 603
Krajnović D. et al., 2008, MNRAS, 390, 93
Kruk S. J. et al., 2018, MNRAS, 473, 4731
Laurikainen E., Peletier R., Gadotti D., 2016, Galactic Bulges (Astrophysics and Space Science Library, Vol. 418). Springer, Berlin
Law D. R. et al., 2016, AJ, 152, 83
Law D. R. et al., 2021, AJ, 161, 52
Lelli F., McGaugh S. S., Schombert J. M., Desmond H., Katz H., 2019, MNRAS, 484, 3267
Liu F. T., Ting K., Zhou Z.-H., 2012, ACM Trans. Knowl. Discov. Data, 6, 1
Mendel J. T., Simard L., Palmer M., Ellison S. L., Patton D. R., 2014, ApJS, 210, 3
Moster B. P., Naab T., White S. D. M., 2018, MNRAS, 477, 1822
Nanni L. et al., 2022, MNRAS, 515, 320
Navarro J. F., Frenk C. S., White S. D. M., 1996, ApJ, 462, 563
Nelson D. et al., 2019, MNRAS, 490, 3234
Noordermeer E., Verheijen M. A. W., 2007, MNRAS, 381, 1463
Oh S. et al., 2016, ApJ, 832, 69
Pak M., Lee J. H., Oh S., D'Eugenio F., Colless M., Jeong H., Jeong W.-S., 2021, ApJ, 921, 49
Peng C. Y., Ho L. C., Impey C. D., Rix H.-W., 2002, AJ, 124, 266
Pillepich A. et al., 2019, MNRAS, 490, 3196
Rigamonti F., Dotti M., Covino S., Haardt F., Landoni M., Del Pozzo W., Lupi A., Zibetti S., 2022a, BANG: BAyesian decomposiotioN of Galaxies, Astrophysics Source Code Library, record ascl: 2205.022
Rigamonti F., Dotti M., Covino S., Haardt F., Landoni M., Del Pozzo W., Lupi A., Zibetti S., 2022b, MNRAS, 513, 6111
Schwarzschild M., 1979, ApJ, 232, 236
Simard L. et al., 2002, ApJS, 142, 1
Skilling J., 2004, in Fischer R., Preuss R., Toussaint U. V.eds, AIP Conf. Proc. Vol. 735, Bayesian Inference and Maximum Entropy Methods in Science and Engineering. Am. Inst. Phys., New York, p. 395
Stetson P. B., 1987, PASP, 99, 191
Strauss M. A. et al., 2002, AJ, 124, 1810
Tabor M., Merrifield M., Aragón-Salamanca A., Cappellari M., Bamford S. P., Johnston E., 2017, MNRAS, 466, 2024
Tabor M., Merrifield M., Aragón-Salamanca A., Fraser-McKelvie A., Peterken T., Smethurst R., Drory N., Lane R. R., 2019, MNRAS, 485, 1546
Thater S. et al., 2022, A&A, 667, A51
Tully R. B., Fisher J. R., 1977, A&A, 54, 661
van den Bosch R. C. E., van de Ven G., Verolme E. K., Cappellari M., de Zeeuw P. T., 2008, MNRAS, 385, 647
Vázquez-Mata J. A. et al., 2022, MNRAS, 512, 2222
Veitch J., Del Pozzo W., 2017, Johnveitch/Cpnest: Pypi Release
Wake D. A. et al., 2017, AJ, 154, 86
Weiner B. J. et al., 2006, ApJ, 653, 1027
Westfall K. B. et al., 2019, AJ, 158, 231
White S. D. M., Rees M. J., 1978, MNRAS, 183, 341
Yan R. et al., 2016, AJ, 151, 8
Zana T. et al., 2022, MNRAS, 515, 1524
Zhu L. et al., 2018a, Nat. Astron., 2, 233
Zhu L. et al., 2018b, MNRAS, 473, 3000
Zhu L., van de Ven G., Méndez-Abreu J., Obreja A., 2018c, MNRAS, 479, 945
Zibetti S., Charlot S., Rix H.-W., 2009, MNRAS, 400, 1181

APPENDIX A: SCALING RELATION WITH DOUBLE SLOPES

We present here the result of a fit on the $M_\star(R_e) - S_{0.5}(R_e)$ with two slopes (Fig. A1). Equation (A1) represent the functional form that we used for the fit, while the best-fitting parameters are reported in Table A1. The evidence of the 'two slopes' model is $\log Z = 20\,516$ against $\log Z = 20\,336$ for the single slope fit

$$\log_{10}\left(\frac{S_{0.5}(R_e)}{100\ \mathrm{km\,s^{-1}}}\right) = \begin{cases} a_1 + b_1 \log_{10}\left(\frac{M_\star}{10^{10.5}\ \mathrm{M_\odot}}\right) \\ \qquad\qquad \text{if} \quad \log_{10}\left(\frac{M_\star}{10^{10.5}\ \mathrm{M_\odot}}\right) \leq M_0 \\ a_2 + b_2 \log_{10}\left(\frac{M_\star}{10^{10.5}\ \mathrm{M_\odot}}\right) \\ \qquad\qquad \text{if} \quad \log_{10}\left(\frac{M_\star}{10^{10.5}\ \mathrm{M_\odot}}\right) > M_0, \end{cases} \tag{A1}$$

where the two constants a_1 and a_2 are not independent of each other due to the continuity condition of the function in M_0.

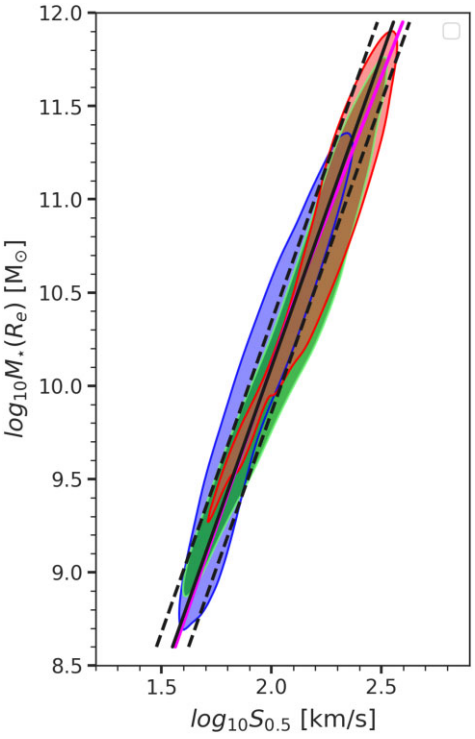

Figure A1. Same as the central panel of Fig. 7. The black solid line is the best linear fit (i.e. Table 4) while the dashed lines represent the one-σ confidence intervals. The fuchsia line is the result of a fit assuming two slopes (i.e. equation A1) whose best-fitting parameters are presented in Table A1.

Table A1. Summary table of the best-fitting parameters for the fit to the $M_\star(R_e) - S_{0.5}(R_e)$ with the functional form of equation (A1).

a_1	a_2	b_1	b_2	M_0
0.12 ± 0.01	0.12 ± 0.01	0.29 ± 0.01	0.32 ± 0.01	10.57 ± 0.01

APPENDIX B: ANALYSIS ON A GALAXY SUBSAMPLE

In this section, we partially repeat the analysis outlined in Section 6 on a galaxy subsample selected discarding all galaxies with $\log_{10}M_\star < 9.5$ and whose bulge half-mass radius is smaller (within its error) than the pixel resolution. We moreover visually inspected and discarded all the objects including ongoing mergers or other contaminants (i.e. wrong redshift, central non-masked stars, and type I AGN).

As shown in Fig. B1 the distribution of 'hot', 'cold', and total masses show similar trends to the one mentioned in the main body of the text (see Section 6 with ellipticals dominating the high-mass regime with a dominant contribution of the 'hot' component and spirals being colder and skewed to slightly smaller masses. The main difference from Fig. 5 is the missing peak at small stellar masses ($\log_{10}M_{\rm hot} \simeq 9.4$) in spirals mostly due to the exclusion of low mass ($\log_{10}M_\star < 9.5$) galaxies.

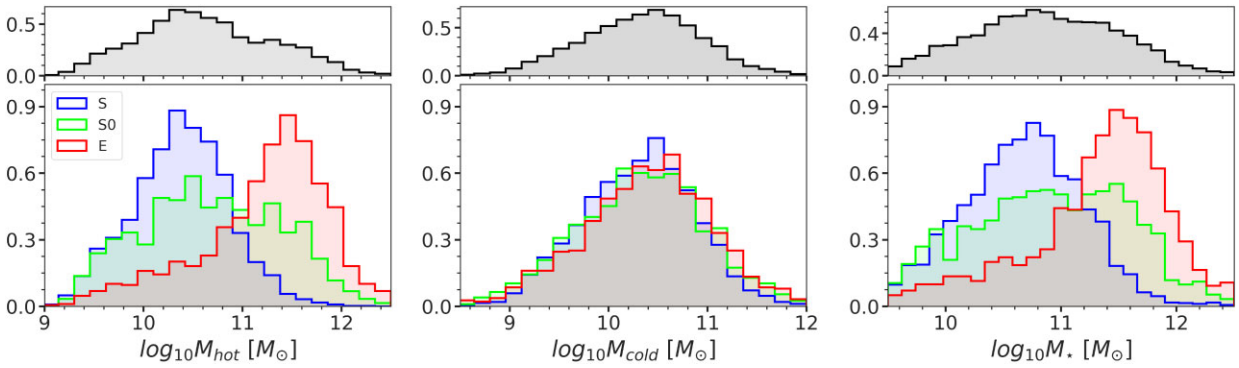

Figure B1. From left to right we show the mass distribution of the hot, cold, and total stellar mass for the sample under analysis. The hot and cold mass are estimated following equations (11) and (12) for the sample selected according to the text ($\simeq$ 5 500 galaxies). Each histogram is normalized to have a total area equal to one, and the distributions are colour-coded according to visual morphology: blue for spirals, green for lenticulars, and red for ellipticals. The panel over each picture represents the distribution of that variable for the whole population helping in understanding the relative role of the three morphological types.

APPENDIX C: SCALING RELATIONS IN THE HALO-FREE CONFIGURATION

We report in this section a summary of the same analysis detailed in Section 5 in the case of the halo-free configuration (see Section 3.2). Tables C1 and C2 report the best-fitting parameters of a linear fit to the data, whose results are roughly comparable (within two σ errors) to the one reported in the halo-fixed configuration (Tables 4 and 5). Fig. C1 shows the same quantities as Fig. 7 for the halo-free case. Some differences can be seen, especially in the low mass regime, where, as expected, the priors on the halo parameters are more informative. The fuchsia line represents the best-fitting linear relation in the halo-fixed configuration which is compatible (within one$-\sigma$ scatter) with the best-fitting line in the halo-free case (black solid line).

Table C1. Summary table of the best-fitting parameters for the linear fit (equations 14, 16) of the kinematic tracers presented in the middle and left-hand panels of Fig. C1. The first column refers to the considered dependent variable (the independent variable is always $M_\star(R_e)$), while the other three columns are the free parameters of the fit, namely, the intercept (a), the slope (b), and the intrinsic scatter σ.

y-axis	a	b	σ
$\log_{10}S_{0.5}(R_e)$	0.15 ± 0.01	0.26 ± 0.01	0.088
$\log_{10} V_{R_e}/k_{R_e}$	0.26 ± 0.01	0.26 ± 0.01	0.081

Table C2. Same as Table C1 but for a subsample of $\simeq$ 7000 galaxies selected according to the same criteria applied in Aquino-Ortíz et al. (2020) (see par. 7 for further details).

y-axis	a	b	σ
$\log_{10}S_{0.5}(R_e)$	0.15 ± 0.01	0.27 ± 0.01	0.076
$\log_{10} V_{R_e}/k_{R_e}$	0.27 ± 0.01	0.27 ± 0.01	0.065

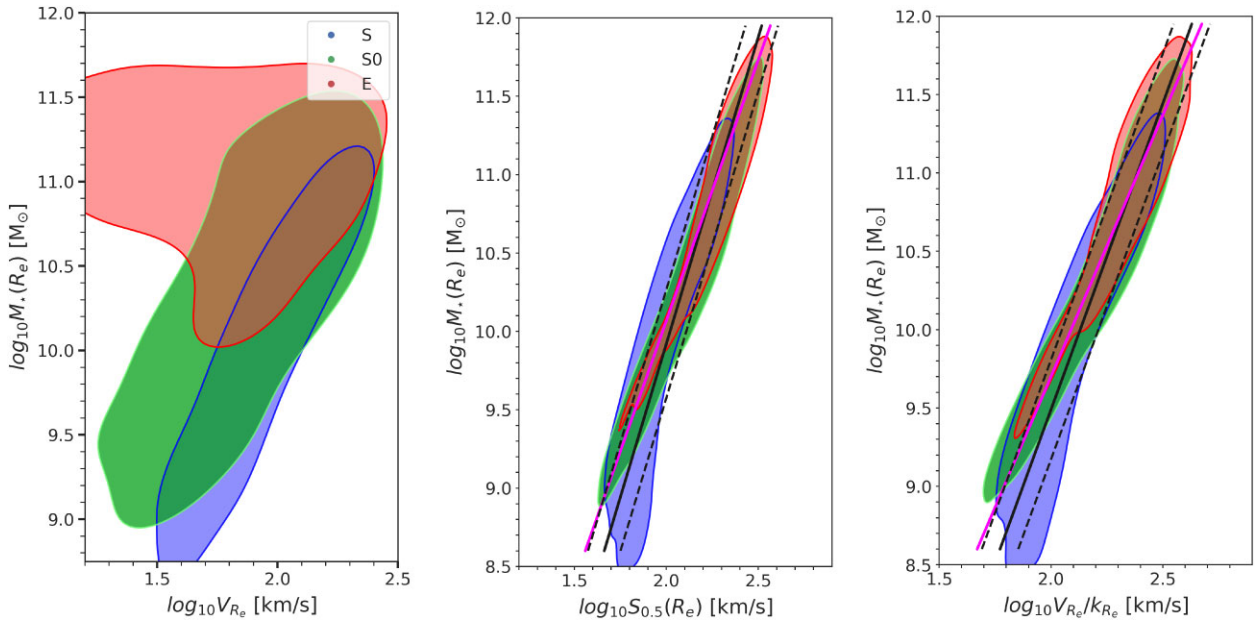

Figure C1. Scaling relations of different kinematics tracers divided according to morphology (blue for spirals, green for lenticulars, and red for ellipticals) in the case of the halo-free configuration. In all three plots, the y-axis is the logarithm of the stellar mass within one R_e, while the horizontal axis, respectively from left to right, shows the logarithm of the velocity at oneR_e (V_{R_e}), the logarithm of the $S_{0.5}$ parameter (see equation 13) and the logarithm of the velocity at R_e corrected according to equation (15). Density contours respectively contain 75 per cent, 80 per cent, and 80 per cent of the kernel density estimated probability mass. The solid black lines are the best-fitting linear relations while the black dotted lines represent the one $-\sigma$ confidence interval, and the fuchsia line is the best-fitting relation computed from Table 4. The best-fitting parameters are summarized in Table C1.

This paper has been typeset from a TEX/LATEX file prepared by the author.